Journal of Turbomachinery. Received May 20, 2026;
Accepted manuscript posted August 10, 2026. doi:10.1115/1.4072497

Assessment of the Delayed Detached-Eddy Simulation Method for Predicting Off-Design Operating Conditions of an Axial Compressor

Felix M. Möller[1]
Institute of Test and Simulation
for Gas Turbines,
German Aerospace Center (DLR),
Cologne 51147, Germany
email: felix.moeller@dlr.de

Christian Morsbach
Institute of Propulsion Technology,
German Aerospace Center (DLR),
Cologne 51147, Germany

Paul G. Tucker
Department of Engineering,
The University of Cambridge,
Cambridge CB2 1PZ, United Kingdom

Zhong-Nan Wang
College of Engineering and Physical Sciences,
The University of Birmingham,
Birmingham B15 2TT, United Kingdom

Florian Herbst
Institute of Propulsion Technology,
German Aerospace Center (DLR),
Cologne 51147, Germany

Reliable, highly accurate prediction of off-design operating conditions using numerical methods is essential for overcoming the challenges of achieving greener aviation. To assess their capabilities, the high-speed TU Darmstadt axial compressor stage is considered at near stall conditions. Steady Reynolds-averaged Navier-Stokes (RANS) methods fail to capture the unsteady flow physics. Hence, the results show large deviations from experimental reference data. This was investigated by a comprehensive pre-study involving the variation of the mesh density, turbulence model extensions and operating point control mechanisms. Improvements were seen when using unsteady methods such as unsteady RANS (U-RANS) or the Delayed Detached-Eddy Simulation (DDES). Both methods show much closer agreement with the experiment while DDES outperforms U-RANS. These improvements were found to be due to the fact that DDES resolved both the deterministic and stochastic scales of the unsteady flow field, especially in separated flow regions. Further, a thorough assessment of two mechanisms to control the unsteady operating point near stall, namely the mass flow controller and a converging-diverging nozzle, was done. The mass flow controller performed best in terms of operability, predictive accuracy and reduced requirements on a priori knowledge from pre-cursor RANS simulations. The DDES method showed its potential and represents a powerful approach to investigating unsteady off-design operating conditions with high accuracy (below 1% average relative error in radial profiles of the total pressure and temperature ratio, as well as the circumferential flow angle).

Keywords: Turbulence Modeling, Hybrid RANS/LES, Delayed Detached-Eddy Simulation, Axial Compressor Stage, Off-design

1 Introduction

To address the challenges towards greener aviation, such as increased efficiency and a wide and safe operating range of the jet engine, the industrial design process requires affordable, yet highly accurate computational fluid dynamics (CFD) methods. Having these methods at hand allows for faster design cycles and, consequently, a faster entry-into-service, which reduces the environmental footprint of aviation. At the aerodynamic design point (ADP) and peak efficiency (PE), steady state-of-the-art Reynolds-averaged Navier-Stokes (RANS) methods are widely used and constitute a reliable method in the design process. Moving away from these conditions and approaching off-design conditions near stall (NS) still poses a substantial challenge for steady RANS methods [1–3]. As these operating points are characterized by high unsteadiness, steady methods fail and cannot be used reliably. Nevertheless, it is of utmost importance to predict this region in a compressor performance map with best accuracy to determine safe operating ranges and safety margins.

This could, in principle, be addressed with the high-fidelity large-eddy simulation (LES) method, which is a very powerful but computationally expensive alternative to deal with these challenging conditions and to increase the numerical accuracy. Its potential for turbomachinery applications has been shown in the recent past [4–7], while these applications are limited to prismatic blades with spanwise periodicity, single blade passages with end-walls and basically low Reynolds numbers. Increasing the Reynolds number or extending the numerical domain to multiple blade rows remarkably increases the computational costs, which limit the application range of LES, to date.

A popular compromise between accuracy and costs is hybrid RANS/LES (HRL) approaches. In this work, we focus on the delayed detached-eddy simulation (DDES) method, which is a seamless approach blending between unsteady RANS (U-RANS)- and LES-like behavior inherently aiming to resolve turbulent structures in the separated flow regions. This approach has shown its potential for large-scale configurations at off-design in the past. The inception of rotating stall was investigated in a full annulus rotor-stator compressor stage [8] and a multi-stage configuration [9]. Both derived important findings for the stall mechanism based on their computational results. Further, Scheibel et al. considered a 45° segment of a rotor-stator compressor setup [10] and a full-annulus rotor configuration [11], showcasing the potential of predicting pre-stall conditions with DDES. Patel et al. [12] used this hybrid method to analyze the non-synchronous vibration (NSV) mechanism in a 1.5 stage axial compressor and summarized that the hybrid approach captured relevant NSV frequencies. These references represent only a small selection of recent applications of DDES to highly unsteady compressor flows at off-design conditions, which motivate the further investigation of this method.

In order to evaluate the predictive capabilities of DDES, we examine a compressor stage under off-design conditions and compare

[1]Corresponding Author.
Version 1.18, June 25, 2026

Journal of Turbomachinery. Received May 20, 2026;
Accepted manuscript posted August 10, 2026. doi:10.1115/1.4072497

the results with those obtained from the experiment, as well as from steady RANS and U-RANS simulations. To meet the specified operating point, different control mechanisms will be introduced and discussed for all numerical methods. Especially at unsteady near stall conditions, the operating point control is an essential aspect to ensure comparability with measured flow conditions.

Based on this, and within the scope of this work, our aim is to answer the following research questions:

- What are the limitations of steady RANS methods in predicting near stall conditions of a compressor stage?
- Is the DDES method capable of increasing the predictive accuracy compared to steady and unsteady RANS and where are its limitations?
- What mechanisms exist to control a near stall operating point numerically and is there a preferred approach?

2 Test case description

To assess the predictive capabilities of CFD methods, and especially DDES, near stall, the transonic TU Darmstadt axial compressor stage (TUDa)[2] is investigated at 65 % speed. This represents a corrected speed of $N_{\mathrm{corr}} = 13\,000$ rpm, which is corrected to international standard atmosphere (ISA) conditions. The real speed to be used for the simulations can be derived by

$$N_{\mathrm{real}} = N_{\mathrm{corr}} \sqrt{\frac{T_{\mathrm{t,15}}}{T_{\mathrm{ISA}}}} \quad (1)$$

with the reference temperature $T_{\mathrm{ISA}} = 288.15\,\mathrm{K}$ and the integral area-averaged total temperature at ME15. The real mass flow, specifying the operating point, is obtained by

$$\dot{m}_{\mathrm{real}} = \dot{m}_{\mathrm{corr}} \frac{p_{\mathrm{t,15}}}{p_{\mathrm{ISA}}} \sqrt{\frac{T_{\mathrm{ISA}}}{T_{\mathrm{t,15}}}} \quad (2)$$

with the reference pressure $p_{\mathrm{ISA}} = 101\,325\,\mathrm{Pa}$ and the integral area-averaged total pressure at ME15. In the following, the corrected mass flow is normalized by its value in the ADP at 100 % speed yielding $\dot{m}_{\mathrm{corr,rel}} = \dot{m}_{\mathrm{corr}}/16\,\mathrm{kg/s}$.

The experimental setup consists of 16 rotor blades and 29 stator vanes and we consider the blade version combination *R1S7*. The stator *S7* has been optimized by Bakhtiari et al. [13] to avoid flow separation on the stator suction side at design speed. The specified rotor tip-gap size is 8×10^{-4} m, which is also used in the numerical setup. A comprehensive summary and description of the experiment, as well as applied measurement techniques and measured operating points is given by Klausmann et al. [14,15]. Four measurement planes (MEs), namely ME15, ME20, ME21 and ME30 are provided, which represent locations far upstream the spinner nose, upstream the rotor, downstream the rotor and downstream the stator, respectively. This allows for a comprehensive comparison between experimental and numerical results. ME15 and ME20 are not considered in isolation but are used as reference planes and to extract reference values. Figure 1 shows the experimentally measured performance map for 65 % speed, characterized by the stage total pressure ratio $\Pi_{\mathrm{t,30\text{-}15}}$ and the isentropic efficiency η_{is}. The peak efficiency and near stall operating points are highlighted as they will be considered numerically in this work.

The Reynolds and Mach number with respect to the blade rows are summarized for the near stall operating point in Tab. 1. It becomes clear that at reduced speed and near stall conditions, the TUDa compressor stage is subsonic, hence, no passage shock occurs. The Reynolds number, especially for the rotor, represents a

[2]the open case is officially provided here: https://gpps.global/data-sets (accessed on 23.06.2026)

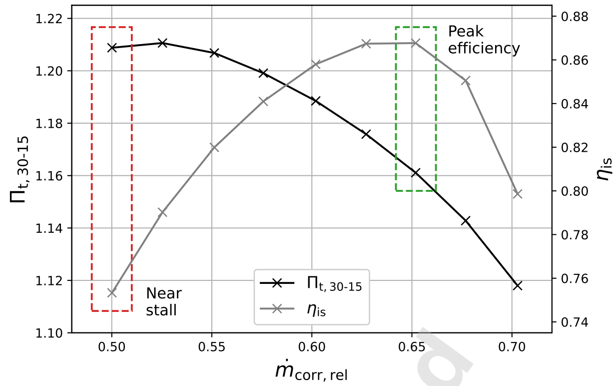

Fig. 1 Experimentally measured performance map for 65% speed showing the stage total pressure ratio and isentropic efficiency for varying relative corrected mass flow rates.

relatively large value, which would require a very fine mesh density for a fully 3D LES of this case. Therefore, it is important to work out how DDES performs in this case and if it is a feasible alternative to increase the predictive accuracy (compared to RANS and U-RANS), but keep computational costs as low as possible (compared to LES).

Table 1 Operating point characteristics for 65% speed and $\dot{m}_{\mathrm{corr,rel}} = 0.5$, which represents near stall conditions (marked in Fig. 1). The required quantities to determine these values are extracted at ME20 and ME21 for the rotor and stator, respectively. This corresponds to inflow conditions for each component. The reference length for each component is the mid-span chord length.

	Rotor	Stator
Reynolds number	1 144 432	462 963
Mach number	0.608	0.413

Numerical setup. The numerical representation of the compressor stage is shown in Fig. 2 and highlighted in blue and green. For steady RANS, a single-passage setup is used with a mixing plane approach [16,17] at the rotor-stator interface, which is known as a common but critical simplification when simulating multi-row configurations. The unsteady setup consists of a single rotor and two stator passages, resulting in a 1:2 interface, treated with a zonal interface [18] and accounting for the unsteady transfer of the rotor wake to the stator domain. To realize this 1:2 interface, the number of stator vanes had to be increased from 29 to 32. It has to be emphasized that this scaling brings a notable change in the solidity (> 10 %), which may impact the aerodynamic results, especially, when considering transonic operating conditions. For the subsonic conditions, analyzed in this work, the aerodynamic effect of this scaling is considered as negligible as was also done by [19,20]. Based on N_{real} and a numerical domain of 1/16 of the full annulus, the characteristic frequency for unsteady simulations $f_{\mathrm{c}} = 3487.48\,\mathrm{Hz}$ can be defined. This represents the frequency with which the rotor passes both stator passages while its reciprocal defines a single period P in the following. The experimental measurement planes are replicated in the numerical setup and used to sample time-resolved data for the unsteady setups. The block-structured meshes were generated with our in-house tool *PyMesh* [21]. The inlet boundary conditions are dictated by the experiment and were measured at ME15 (see Fig. 2). A radial inlet profile containing information about the total pressure and temperature, as well as a uniform inflow velocity vec-

Journal of Turbomachinery. Received May 20, 2026;
Accepted manuscript posted August 10, 2026. doi:10.1115/1.4072497

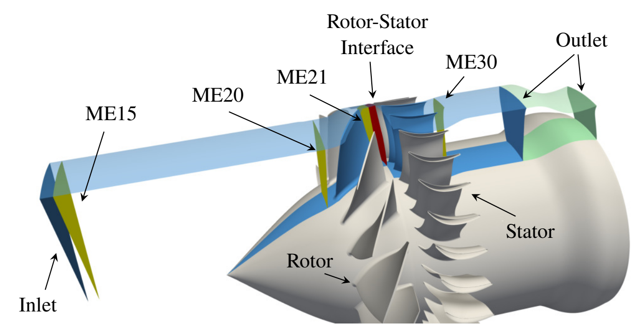

Fig. 2 Numerical domain overview of a single rotor and two stator passages (highlighted in blue). Experimental measurement planes are shown in yellow and the rotor-stator interface is marked by a red plane. The outlet nozzle is indicated by a green domain extension and only used partially (simulations are labeled where used).

tor in x-direction (zero inflow angle in circumferential and radial direction) is prescribed. Additionally, the turbulent state is defined with constant values for the turbulence intensity $Tu = 4\,\%$ and the turbulent length scale $l_t = 9 \times 10^{-5}$ m. The turbulent quantities were not explicitly measured, but officially provided and also used by others [20,22,23]. The outlet was treated differently, depending on the operating point control approach, which will be introduced in Sec. 3.3.

3 Methodology

3.1 Numerical methods. All simulations have been conducted with the DLR turbomachinery solver *TRACE*[3], which has been continuously developed and validated at the Institute of Propulsion Technology in the Department for Numerical Methods [24,25] in close collaboration with MTU Aero Engines AG. The 2nd order accurate density-based cell-centered finite-volume solver of *TRACE* was used. All unsteady simulations were conducted with a 3rd order accurate implicit Runge-Kutta scheme [26] with a dual-time marching scheme. The physical time step is given by

$$\Delta t = \frac{1}{f_c \, n_{\text{tspp}}} \tag{3}$$

with the defined number of time steps per period n_{tspp}. The DDES were conducted with $n_{\text{tspp}} = 2048$ to guarantee a sufficiently small time step for stable simulations. U-RANS simulations are less demanding in terms of the time step size, hence, they were partly conducted with a larger time step using $n_{\text{tspp}} = 1024$ (still resulting in a relatively small time step size for industrial U-RANS setups).

3.2 Turbulence models. In alignment with previously conducted studies for the TUDa compressor stage at design speed ($N_{\text{corr}} = 100\,\%$) [27], we consider steady and unsteady RANS, as well as DDES, based on the two-equation Menter-SST turbulence model [28] in combination with the one-equation γ-transition model [29]. Although the effect of laminar-to-turbulent transition is marginal and especially near stall, fully turbulent and massively separated flow conditions are expected, we strive to comprehensively assess the transitional DDES for various flow conditions. To be consistent with previous studies [27,30–32], this transitional model version will also be considered in this work.

Specific DDES model settings. The DDES model is used in its version of Spalart et al. [33]. To control the switch between U-RANS- and LES-mode, the vorticity-based sub-grid length scale (SLS) approach by Shur et al. [34] is used, which is beneficial compared to the standard grid-based SLS and notably accelerates the transition from modeled to resolved scales. In our case, the solver blending σ_b by Travin et al. [35] is modified. Originally, this method automatically blends between the central ($\sigma_b = 0$) and Roe upwind [36] ($\sigma_b = 1$) formulation of the Riemann solver to compute the inviscid fluxes. It was found that for the compressor case including unsteady tip leakage flow and at near stall conditions, this approach requires a modification to stabilize the method, resulting in

$$\sigma_{\text{b,mod}} = \max\left(0.5, \sigma_{\text{b,orig}}\right). \tag{4}$$

This ensures at least 50 % amount of upwind flux in each cell, which is favorable for highly unsteady operating points. The required characteristic time t_c for $\sigma_{\text{b,orig}}$ was determined based on the average chord length of the rotor and the area-averaged relative velocity magnitude at ME20. A comprehensive summary and further assessment of the transitional DDES is given in [30–32].

3.3 Operating point control. The operating point for the TUDa compressor stage is defined by the mass flow rate and rotational speed. To achieve comparable conditions for the numerical setup, a suitable control mechanism at the outlet boundary has to be applied. Within this work, we discuss three possible approaches, which are introduced in the following.

Fixed outlet pressure (FOP). Many CFD simulations are controlled by the static outlet pressure with, in our case, a radial equilibrium condition [37], which is imposed at the mid-span of the outlet panel. It is beneficial as there is little controller interaction and for moderate flow conditions, high stability and fast convergence of the results can be achieved with this approach. Nevertheless, a notable weakness of this method of achieving a specific operating point, characterized by the mass flow, is that it requires *a priori* knowledge of the correct outlet pressure that will produce the desired mass flow. While iterations to obtain the correct mass flow are computationally inexpensive for steady RANS simulations, it becomes very costly if multiple iteration loops have to be done for unsteady simulations or rather high-fidelity methods.

Mass flow controller (MFC). To meet the targeted operating point, a P-controller can also be used to control the mass flow rate. In our case, the mass flow controller (MFC) acts proportionally on the control value (static outlet pressure), which is affected by the evaluation value (mass flow). The resulting scaling factor (SF), which is applied to the static outlet pressure boundary condition (BC) value, is determined by

$$\text{SF} = \text{SF}_{\text{previous}} \cdot \left[1 - \phi_{\text{relax}} \cdot \left(\frac{\dot{m}_{\text{out,target}}}{\dot{m}_{\text{out,actual}}} - 1\right)\right] \tag{5}$$

where a relaxation factor $\phi_{\text{relax}} = 0.2$ was used. For the unsteady simulations, the evaluation and control values are averaged over a single period P. Further, it was found, that the controller acted unfavorably if it was active from the beginning of an unsteady simulation starting from a steady RANS initial solution. Hence, to stabilize the flow state, the controller was first activated after three periods. When restarting the simulation, again, an immediate controller intervention was avoided by defining its activation after half of a period.

Converging-diverging nozzle (CDN). Another mechanism to control the mass flow of the compressor stage is adding a converging-diverging nozzle (CDN) at the domain outlet, as was

[3] https://trace-portal.de/userguide (accessed on 23.06.2026)

Journal of Turbomachinery. Received May 20, 2026;
Accepted manuscript posted August 10, 2026. doi:10.1115/1.4072497

also done by [38,39]. This setup increases the computational costs by increasing the number of cells, but, at the same time, is closest to actual experimental setup [15]. At the test facility, this operating point is also controlled by an outlet nozzle. Numerically, it is aimed to reach Ma = 1.0 in the critical cross-section A_{crit} of the nozzle with subsequent supersonic flow in the divergent part. As a result, the mass flow of the compressor stage is mainly determined by the compressor aerodynamics and the critical cross-section and not by a fixed outlet boundary condition. The latter faces supersonic outflow conditions, which reduce the requirements for the BC. We use our pre-processor *PREP* (also part of the *TRACE* suite) to define the surface deformation[4] by following the steps below:

(1) Extract integral area-averaged quantities at the outlet panel from a simulation without nozzle (blue domain in Fig. 2)
(2) Determine the critical cross-section of the CDN, which can be derived from ideal gas relations with

$$A_{\mathrm{crit}} = \frac{A\ \mathrm{Ma}}{\left[1 + \frac{\kappa-1}{\kappa+1}\left(\mathrm{Ma}^2 - 1\right)\right]^{\frac{\kappa+1}{2(\kappa-1)}}} \tag{6}$$

where A is the cross-section and Ma the Mach number at the outlet panel of the baseline configuration without the nozzle. The heat capacity ratio is $\kappa = 1.4$.
(3) Compute the radial surface displacement $\delta(x)$ of the lower and upper wall (illustrated in Fig. 2) in the green domain by

$$\delta(x) = \begin{cases} \frac{\delta_{\mathrm{center}}}{2}\left[1 + \cos\left(\pi \frac{x_{\mathrm{center}} - x}{x_{\mathrm{center}} - x_{\mathrm{start}}}\right)\right] & \text{if } x < x_{\mathrm{center}} \\ \frac{\delta_{\mathrm{center}}}{2}\left[1 + \cos\left(\pi \frac{x - x_{\mathrm{center}}}{x_{\mathrm{end}} - x_{\mathrm{center}}}\right)\right] & \text{if } x \geq x_{\mathrm{center}} \end{cases} \tag{7}$$

where the radial displacement in the critical cross-section of $\delta_{\mathrm{center}} = 0.01969\,\mathrm{m}$ can be determined based on A_{crit} and the assumption of a constant channel height in circumferential direction. The further geometry-related input values are:

- $x_{\mathrm{start}} = 0.015\,\mathrm{m} \rightarrow$ Start of the nozzle shape contouring, beginning downstream the outlet of the configuration without nozzle.
- $x_{\mathrm{end}} = 0.16\,\mathrm{m} \rightarrow$ End of the nozzle shape contouring. In our case this value was defined to be downstream the outlet panel of the setup with a nozzle as this prevents the diverging part to end at $\delta = 0$.
- $x_{\mathrm{center}} = 0.07\,\mathrm{m} \rightarrow$ Axial position of the critical cross-section.

For the additional nozzle domain, the lower and upper wall are defined as slip wall to avoid boundary layer effects in the nozzle itself and at the outlet panel, as well as, the upstream propagation of acoustics from the outlet panel through the subsonic boundary layer.

In the following, we will investigate all three methods to identify their benefits, but also potential pitfalls. Especially, when it comes to the initialization of unsteady setups with poorly conditioned precursor steady RANS results, the control mechanisms potentially reach their limitations.

4 RANS pre-studies

Preliminary studies have been conducted for steady RANS only. This helped to identify the weaknesses of this approach and understand the test case control at off-design conditions. It also provided initial solutions for the unsteady simulations, where they were sensibly usable.

[4]https://trace-portal.de/userguide/prep/page_storyNozzlePreprocess.html (accessed on 23.06.2026)

4.1 Mesh density. To assess the mesh sensitivity of steady RANS, a systematic grid study comprising different grid versions has been conducted. The baseline mesh represents grid factor (GF)=1.0, which is already fine compared to other RANS setups [20,22,23]. This is why mostly coarser meshes were generated to 'challenge' the steady approach. The conducted coarsening/refinement follows the logic of globally multiplying the baseline grid points (GF=1.0) by the respective grid factor in each direction, which results in an effective coarsening/refinement factor of $\approx \mathrm{GF}^3$ (minor deviations in the actual cell count can be explained with restrictions of the applied meshing tool and its underlying templates). A unified first wall-normal distance was realized to guarantee a non-dimensional cell size $\eta^+ \leq 1$ for all grid factors. Table 2 summarizes the considered mesh densities. The *Ultra-fine* mesh resulted from a previous DDES study and was also taken into account for parts of this study.

Table 2 Summary of considered mesh densities for RANS pre-studies.

Grid factor (GF)	$n_{\mathrm{cells,total}}$
0.5	697 184
0.6	1 170 563
0.7	1 874 164
0.8	2 769 078
0.9	3 974 164
1.0	5 384 352
1.1	7 095 192
2.0 - Ultra-fine (DDES-like resolution)	47 547 424

To get a sense for the mesh sensitivity, two operating points (peak efficiency and near stall) are investigated for various grid factors, where the *Ultra-fine* mesh was only considered for NS. For this investigation, the mass flow controller was used to control the respective operating point. The results are summarized in Fig. 3 showing the relative deviation of the stage total pressure ratio with respect to experimental reference data. As commonly known, for moderate flow conditions at peak efficiency, the steady RANS method shows only minor deviations. Regardless of whether coarse or fine resolution is considered, the results show a small but consistent offset from the experiment. This noticeably changes for the more challenging operating point near stall, which is strongly driven by unsteady phenomena and separated flow. In this case, the coarsest mesh (GF=0.5) shows the smallest relative deviation, where, with refined setups, the method converges towards larger deviations ending at a constant value of $\approx -5.15\,\%$. It was interesting to see, that the coarsest setup seems to cancel out the interplay of numerical steady RANS limitations, such as the coarse spatial discretization and model deficiencies, and highly unsteady flow features. This resulted in smaller deviations still be-

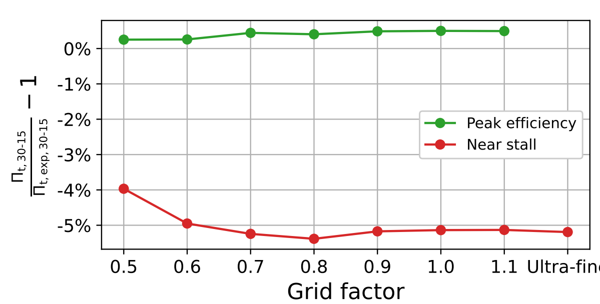

Fig. 3 RANS mesh convergence study for the peak efficiency and near stall operating point (marked in Fig. 1) conducted with the mass flow controller.

Journal of Turbomachinery. Received May 20, 2026;
Accepted manuscript posted August 10, 2026. doi:10.1115/1.4072497

ing 4 % off the experiment. Once the mesh resolution enables the method to "theoretically" capture unsteady scales (this is based on the knowledge, that unsteady DDES simulations are able to resolve turbulent scales at such mesh densities), the failure of the steady approach becomes more apparent and deviations increase. An important finding from this pre-study is that, for near stall conditions, the mesh resolution can have a significant, and even critical impact on the obtained steady RANS results, as well as the conclusions derived from them.

4.2 Turbulence model extensions. There exist a large number of RANS turbulence models extensions, which are developed to address specific limitations of the model and to extend its application range. As summarized in Sec. 3.2, we focus only on the Menter-SST turbulence model [28] (labeled as 'SST'). The investigated extensions are

- the γ-transition model [29] (labeled as 'γ'),
- the stagnation point anomaly fix [40] (labeled as 'SPAF'),
- the rotational effects correction [41] (labeled as 'REC').

We consider different combinations to assess the effect of individual extensions. All simulations have been conducted on the *Ultra-fine* grid (cf. Tab. 2), which was also used for subsequent U-RANS and DDES simulations, to rule out mesh dependencies, and with the mass flow controller. Figure 4 shows the resulting speedlines for the extension combinations. Trends from the preceding mesh study are confirmed. At, and close to, peak efficiency conditions, steady RANS follows experimental results. For near stall conditions $\dot{m}_{\mathrm{corr,rel}} \leq 0.55$, results begin to deviate. The 'closest' agreement at these conditions can be achieved with an extension combination of the stagnation point anomaly fix and rotational effects correction or the transition model. At the same time, each extension yields larger deviations when used standalone. Another interesting finding is, that the plain Menter-SST model outperforms the standalone model extensions for the given mesh resolution. Only a mixed combination shows a total pressure ratio that is closer to that observed in the experiment. Furthermore, it was found, that the usage of a transition model, combined with the stagnation point anomaly fix, does not negatively affect the results. As motivated above (see Sec. 3.2), we investigated the DDES coupled with the γ-transition model in previous studies, which is why we focus only on this model combination in the following.

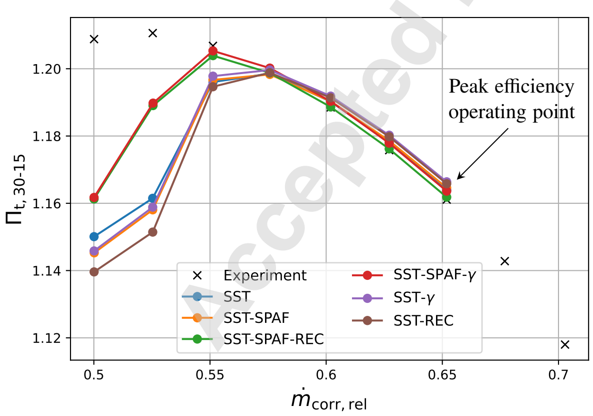

Fig. 4 Compressor map for varying turbulence model extensions resulting from steady RANS simulations with a mass flow controller and for the *Ultra-fine* mesh resolution (see Tab. 2).

4.3 Operating point control mechanisms. The control of highly unsteady operating points is challenging. In Sec. 3.3, we summarized different approaches to do this, which we first investigate with the steady RANS model combination with the transition model and the stagnation point anomaly fix (labeled SST-SPAF-γ in Fig. 4). Besides the variation of the control mechanism, we also included different mesh densities for parts of the study, shown in Fig. 5. The results for the mass flow controller (shown in the zoomed box at ①) have already been discussed in Fig. 3, but are shown here for the sake of completeness. The resulting static back pressure values from these simulations have been used for the simulations with a fixed outlet pressure (FOP) and are shown with squared symbols (□) in Fig. 5 (see zoomed box at ②). These results highlight the ambiguous state for steady RANS as these simulations converge towards a different mass flow rate, far away from the targeted NS operating point, even though the static outlet pressure was extracted from RANS simulations with the MFC at $\dot{m}_{\mathrm{corr,rel}} = 0.5$. Afterwards, it was tried to increase the back pressure iteratively to travel along the experimental speedline towards near stall conditions (indicated by ⋆ symbols). These simulations were conducted for GF=0.8 only. The last stable operating point is at $\dot{m}_{\mathrm{corr,rel}} \approx 0.57$. Behind this point, which means for simulations with even higher back pressure, all results collapse to $\Pi_{t,30\text{-}15} < 1.07$ and $\dot{m}_{\mathrm{corr,rel}} < 0.125$ (points not included in Fig. 5) representing an unphysical flow state. It can be concluded, that with a FOP, this near stall operating point cannot be computed. Lastly, the converging-diverging nozzle setup was tested for GF=1.0 only and is shown with a + symbol (see zoomed box at ①). The mass flow rate is met well, whereas a significant improvement in the total pressure ratio could not be achieved with this method.

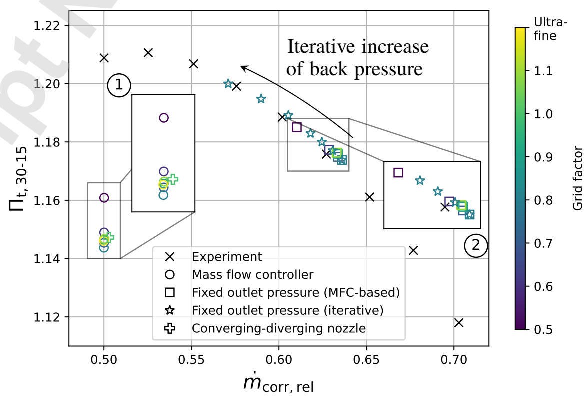

Fig. 5 Resulting stage total pressure ratios for different ways of controlling the near stall operating point for steady RANS and varying mesh densities. The iterative increase of the static back pressure was conducted with GF=0.8. The nozzle setup was computed for GF=1.0 only.

To explain the different results, we show the control and evaluation values of all three operating point control mechanisms at the outlet panel over the number of computed time steps in Fig. 6. They are shown for GF=1.0. A different resulting mass flow rate can be seen. Additionally, the oscillating results for MFC and CDN (seen in the zoomed boxes) are apparent while they show a good agreement with the targeted mass flow rate $\dot{m}_{\mathrm{corr,rel}} = 0.5$. These oscillations are not seen with FOP, indicating a better converged flow solution. As described above, the resulting static outlet pressure from MFC was prescribed for the FOP simulations. This is reflected by the trend of $p_{\mathrm{s,out}}/p_{\mathrm{t,15}}$, showing identical results for all three approaches. The trend of the outlet velocity explains the mass flow deviations. The reference velocity was set to $u_{\mathrm{ref}} = 92\,\mathrm{m/s}$ to still see the differences between the approaches. Using a reference velocity from ME15 would result in identical ratios, as the

Journal of Turbomachinery. Received May 20, 2026;
Accepted manuscript posted August 10, 2026. doi:10.1115/1.4072497

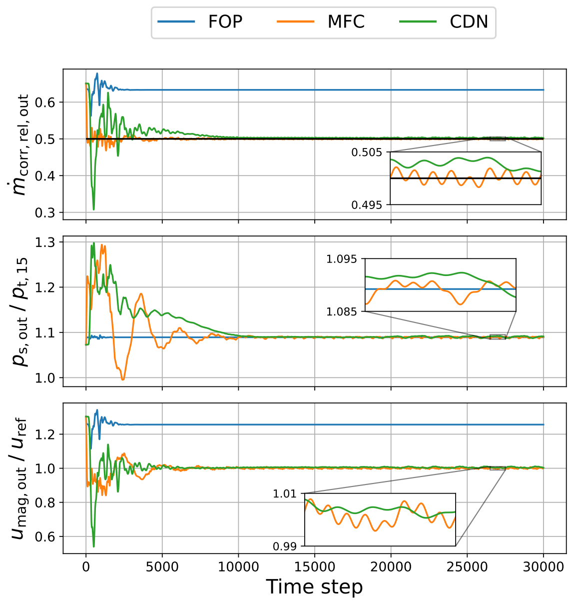

Fig. 6 Convergence of evaluation and control values at the outlet panel for all operating point control mechanisms. Results are shown exemplarily for GF=1.0 (see Tab. 2). The solid black line in the mass flow subplot indicates the target value.

contributed work of the rotor is constant for all simulations. For MFC and CDN, the outlet velocity and dynamic pressure p_{dyn} are controlled by the target mass flow. With the constant work of the rotor, the dynamic pressure at the inlet can be derived and with the given total pressure at the inlet, the static pressure is computed by $p_{\mathrm{s,in}} = p_{\mathrm{t,in}} - p_{\mathrm{dyn,in}}$, which further dictates the static outlet pressure. Consequently, this value depends on the given mass flow rate and the inlet total pressure and cannot develop independently. When using a fixed outlet pressure, derived from MFC, the dynamic pressure is an aerodynamic result of the RANS model and not dictated by the mass flow. Therefore, it depends on the model capabilities to capture this near stall operating point and converges towards a different flow state. Supplementary comments on the convergence of these steady RANS simulations are given in Appendix A.

All three steady RANS pre-studies produced crucial findings for the subsequent investigations with unsteady methods. It became clear, that the near stall operating point cannot be reliably computed with the steady method. The mesh refinement yields even larger deviations to experimental reference data, but converged towards a constant value, which emphasizes the need of finer RANS meshes at near stall conditions. The different control mechanisms revealed, that a fixed outlet pressure cannot be used for this operating point.

5 Comparison of unsteady methods

This section focuses on the comparison of U-RANS and DDES for the near stall operating point only. While the analyses above highlighted the limitations of steady RANS for this highly unsteady operating point, their results are only included in the following where useful. Both unsteady methods have been simulated with the mass flow controller and the converging-diverging nozzle (yielding four unsteady simulations in total). We did not consider unsteady simulations with a fixed outlet pressure, because neither of the RANS pre-cursor simulations yielded a sensible initial value for the outlet BC. It was shown in Sec. 4 that the resulting $p_{\mathrm{s,out}}$ from mass flow controller does not represent an applicable state and the iteration of the outlet pressure already failed at much higher mass flow rates. As a consequence, a back pressure iteration would be required for the unsteady simulations as well, which was not planned for this study.

To avoid the impact of different mesh resolutions, all unsteady simulations have been conducted on the same mesh, summarized in Tab. 3. The mesh resolution in the tip gap has been increased, compared to the steady RANS setups, to better capture its flow physics. Consequently, the resulting number of cells is even higher than for the *Ultra-fine* mesh, summarized in Tab. 2. We ensure a wall-normal spacing $\eta^+ < 0.6$ to meet the low-Reynolds wall treatment requirements. $\Delta\xi^+$ and $\Delta\zeta^+$ are the maximum streamwise and radial non-dimensional cell sizes, respectively, and follow the recommended resolution for hybrid RANS/LES methods [32,42], where the radial resolution is at the upper border.

5.1 Global operating point. The results for all unsteady simulations are shown in the compressor map in Fig. 7. Following the averaging procedure in the experiment, the total pressure ratio $\Pi_{\mathrm{t,30\text{-}15}}$ is computed based on the area-averaged quantities at the respective measurement planes. Furthermore, the quantities of the unsteady simulations are temporally averaged before the total pressure, its ratio and the area-average are computed. In addition to the unsteady simulations, we add the previously discussed various RANS results for the MFC and CDN as an orientation. Focusing on the MFC results, it becomes clear that not only DDES, but already U-RANS notably improves the prediction of the stage total pressure ratio. This clearly indicates the need for an unsteady approach to capture relevant physics of such a near stall operating point. The DDES gets even closer to the experiment, while showing a moderately increased statistical error of the mass flow. The error was determined based on the method described in [43]. The CDN results show a good agreement with experiment as well, but reveal a shift towards a different mass flow rate. This can

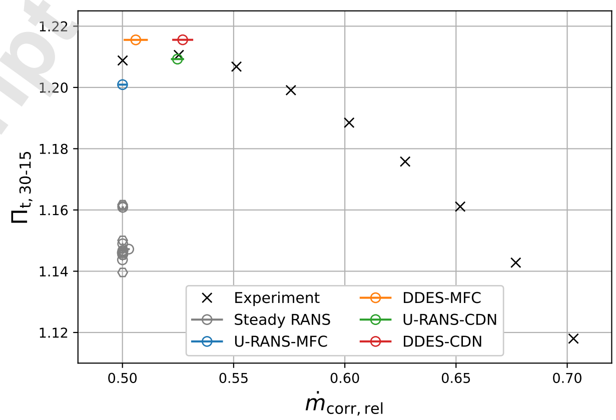

Fig. 7 Compressor map showing the different unsteady numerical methods and operating point control mechanisms. Horizontal lines indicate the statistical error of the mass flow with a 95% confidence interval. Steady RANS results are shown for reference.

be better understood by looking at the temporal development of the mass flow in Fig. 8. The deviations from the targeted mass flow increase with the simulation duration converging towards a different operating point. These results were unexpected at first glance as the nozzle was designed to control the exact mass flow by a choked flow in the critical cross-section. An identified weakness in the conducted CDN setup process is the dependency on steady RANS pre-cursor simulations. As described in Sec. 3.3 (Step 1), the required quantities are extracted at the outlet panel from a simulation without nozzle, which was a steady RANS setup in our case. Based on them, the critical cross-section is derived. Choked flow in the nozzle is still guaranteed for the desired flow speed for the unsteady setups, but the mass flow also depends on

Journal of Turbomachinery. Received May 20, 2026;
Accepted manuscript posted August 10, 2026. doi:10.1115/1.4072497

Table 3 Summary of characteristic mesh values for the unsteady setups. The numbers for the individual components represent single passage values. The total numbers in the bottom lines account for the 1:2 setup, hence, the number of cells is doubled downstream the rotor. The cell numbers in streamwise (along the blade surface), radial and pitchwise directions are given for the rotor or stator passage. The non-dimensional cell sizes are maximum values along the respective blade surface.

Component	$n_{cells,total}$	$n_{cells,streamwise}$	$n_{cells,radial}$	$n_{cells,pitchwise}$	$n_{cells,tip\text{-}gap}$	$\Delta\xi^+$	η^+	$\Delta\zeta^+$
Intake	3.93×10^6							
Rotor	19.62×10^6	260	328	192	38	220	< 0.6	380
Stator	20.33×10^6	280		228		200		300
Outlet	3.66×10^6							
Nozzle	2.71×10^6							
Total (MFC)	71.53×10^6							
Total (CDN)	76.95×10^6							

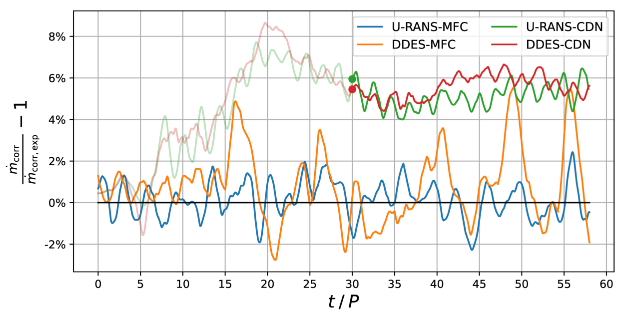

Fig. 8 Temporal development of the integral area-averaged mass flow on the outlet panel of the respective domain with respect to the experimental target mass flow. The CDN setups show a notable initial transient, indicated by grayed-out lines, which is cut off in subsequent investigations. The circled symbol marks the defined end of the initial transient for CDN simulations.

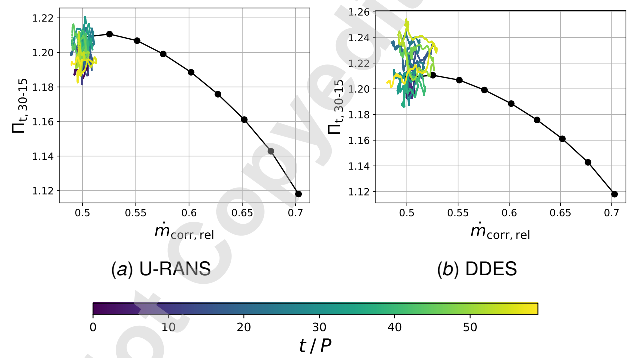

Fig. 9 Illustration of the wandering operating point in the compressor map for the U-RANS and DDES simulation with the mass flow controller.

the fluid density. And since U-RANS and DDES capture the flow field more accurately, this state changes drastically. As a result, the mass flow rate, controlled by the nozzle, changes for the unsteady setups as well. This is an essential finding when we discuss appropriate operating point control mechanisms for unsteady simulations. While we argued, that the FOP approach is not applicable because it requires iterations of the static outlet pressure, we learn, that the nozzle setup also requires more accurate *a priori* knowledge or iterations to determine the nozzle geometry. The latter is the case, if no unsteady results are available to derive the correct critical cross-section. Since we conducted this study in a parallel fashion, we could not benefit from unsteady MFC results to generate a more accurate converging-diverging nozzle. Having a look at the MFC results in Fig. 8 confirms, that the mass flow controller is able to realize the defined mass flow rate. In comparison to U-RANS, DDES shows larger amplitudes, caused by resolving more stochastic scales, but still oscillates around the target value.

The unsteadiness of the considered operating point is illustrated in Fig. 9 for the mass flow controller simulations. We show the temporal development of the total pressure ratio and mass flow for U-RANS and DDES separately. While the temporal average (see Fig. 7) is close to experimental data, the unsteady results significantly ‘travel’ around the mean value, which highlights the dynamics of this off-design operating point.

5.2 Rotor domain. The 3D flow topology in the tip region of the rotor is illustrated in Fig. 10. It shows a top view of the rotor domain for the DDES with a mass flow controller. The instantaneous flow field has been averaged over the last 10 periods to better highlight the essential flow topologies. The resolved scales are shown using the Q-criterion [44] with $Q = 5 \times 10^7\ \mathrm{s}^{-2}$ and colored with the normalized static pressure $p_s/p_{t,15}$. The tip-vortex is initiated at the blade leading edge (see ①). Subsequently, the orientation of the vortex towards the domain passage (indicated with the red arrow, see ②) emphasizes the off-design conditions and illustrates a strongly deviating incidence from design conditions. It becomes clear that the tip vortex does not follow the main flow in streamwise direction anymore, but interacts with the adjacent leading edge. This notable deflection deviates from design conditions and the dynamics of the tip vortex are highly unsteady, which can also be seen in Fig. 11. We show the space-time diagrams for both unsteady simulations (Figs. 11(*a*) and 11(*b*)) at a relative radius $r_{rel} = 0.9$ and for 10 periods. The contours present the phase-averaged normalized static pressure on the rotor pressure side. Close to the leading edge, $0 \leq x/c_{ax} \leq 0.4$, the unsteady motion and interaction of the tip vortex with the adjacent blade pressure side can be seen. Recurring static pressure drops indicate the impingement and oscillation of the vortex core, followed by a short recovery. The resulting pressure contours of the DDES method are more unsteady compared to U-RANS, although the latter also captures a pressure drop close to the leading edge. Further downstream, neither method shows large pressure variations indicating, that the tip vortex only interacts with the upstream part of the blade. In addition, the time-averaged static pressure distribution is compared to steady RANS in Fig. 11(*c*), which further reveals the inabilities of steady RANS to compute this challenging operating point. In the discussed region between $0 \leq x/c_{ax} \leq 0.4$ RANS shows a pressure ratio < 1 (highlighted as red area) which is not seen for the unsteady approaches. It can be concluded that the steady approach has an undesirable effect, decreasing the static pressure locally, which results in a constant backflow at the tip region and is typically not intended by a compressor.

Capturing these unsteady effects is essential and remarkably

Journal of Turbomachinery. Received May 20, 2026;
Accepted manuscript posted August 10, 2026. doi:10.1115/1.4072497

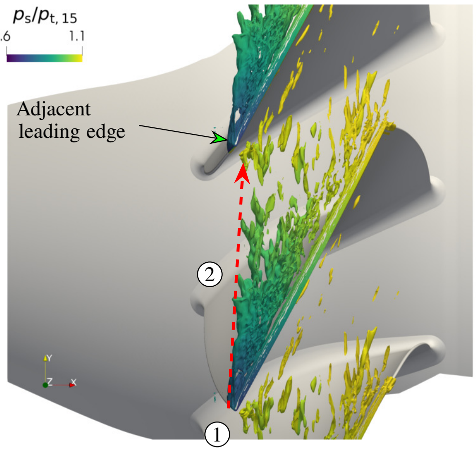

Fig. 10 Top-view of the time-averaged tip-leakage vortex for the DDES conducted with a mass flow controller. Turbulent structures are illustrated by the Q-criterion and colored with the normalized static pressure. Scales occurring below r = 0.18 m are clipped for better illustration. The instantaneous flow field was averaged over the last 10 periods.

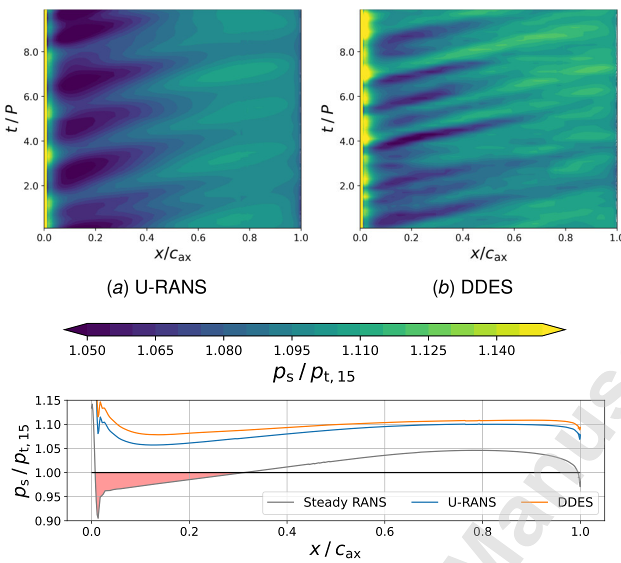

(*a*) U-RANS (*b*) DDES

(*c*) Time-averaged pressure distribution

Fig. 11 Space-time diagram of the normalized static pressure on the rotor pressure side at relative radius = 0.9 for 10 periods and conducted with the mass flow controller. At the bottom, the time-averaged data is compared to steady RANS.

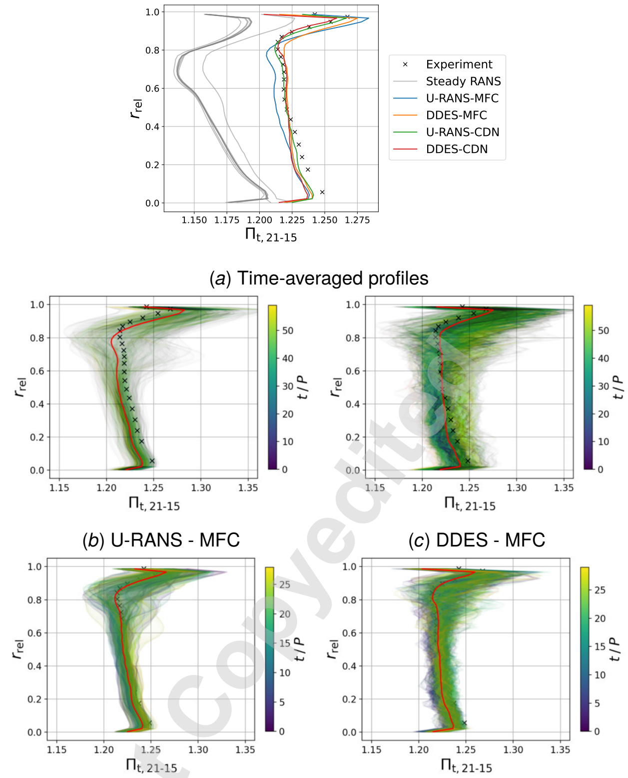

(*a*) Time-averaged profiles

(*b*) U-RANS - MFC (*c*) DDES - MFC

(*d*) U-RANS - CDN (*e*) DDES - CDN

Fig. 12 Circumferentially averaged radial profiles of the total pressure ratio at ME21. (a) shows all temporally averaged results next to each other. (b)-(e) show the temporal evolution for each method separately, while the red solid line represents the time-averaged profile.

improves the prediction accuracy. This is confirmed by the comparison with experimental reference data at ME21 downstream the rotor in Fig. 12. On top (see Fig. 12(*a*)), we show all resulting temporally averaged radial profiles for the unsteady simulations. The previously discussed steady RANS simulations are also shown for different meshes and operating point control mechanisms. A differentiation for these results is not made, as they are just shown to put the improvements of the unsteady approaches into perspective. Focusing on the MFC results, a very good agreement with the experiment can be seen, especially in the tip region ($0.5 \leq r_{\text{rel}} \leq 1.0$). Compared to U-RANS, DDES gets even closer to the experiment. In the hub region, deviations to the experiment are apparent and differences between U-RANS and DDES disappear. This can be explained by the model design of the DDES, which only switches to LES-like behavior in separated regions. In the hub region, the flow is not separated and the DDES behaves identical to U-RANS. For the CDN results, both the U-RANS and the DDES show a very close agreement with the experiment. However, it should be noted that the mass flow slightly deviates (see Fig. 7) from the experimental target value. The temporal variation of these profiles is shown in Figs. 12(*b*) to 12(*e*). The profiles are colored by the number of computed periods, highlighting the unsteadiness of the wake flow. A supplementary comparison of the circumferential flow angle at ME21 is given in Appendix D.

5.3 Stator domain. Moving down the flow path, a comparison of the 3D separated flow field in the stator passage is given by Fig. 13. Both figures show the time-averaged flow field over the last 10 periods obtained with the mass flow controller. The turbulent structures are illustrated with a Q-criterion $= 1 \times 10^7\ \text{s}^{-2}$ and colored by the streamwise vorticity which is given by

$$\omega_{\text{sw}} = \frac{u_i \epsilon_{ijk} \frac{\partial u_k}{x_j}}{\sqrt{u_q u_q}}. \qquad (8)$$

Recalling the fact, that both methods were computed on the exact same mesh, it is impressive to see how much more resolved content is apparent in the DDES. The separation bubble size in radial direction differs between U-RANS and DDES (see different arrow size in Figs. 13(*a*) and 13(*b*)), which indicates that the former overpredicts the separation, resulting in increased total pressure losses downstream the stator, as well as higher blockage and subsequent mass flow redistribution towards the hub.

Capturing a larger amount of resolved turbulent scales (details are shown in Appendix B) increases the accuracy, which is confirmed by the comparison with the experiment. The total pressure

Journal of Turbomachinery. Received May 20, 2026;
Accepted manuscript posted August 10, 2026. doi:10.1115/1.4072497

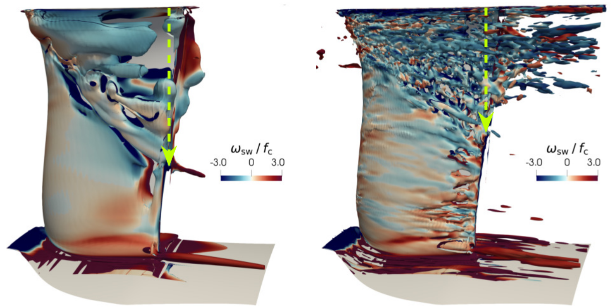

(*a*) U-RANS (*b*) DDES

Fig. 13 Turbulent structures in the stator tip region illustrated by the Q-criterion and colored with the streamwise vorticity. These figures show the results for the mass flow controller and the instantaneous flow field was averaged over the last 10 periods.

ratio $\Pi_{t,30\text{-}15}$ was measured at ME30 (location is illustrated in Fig. 2) and is shown in Fig. 14. Note that the single passage width, indicated by the red dot symbols, is different for the experiment and the numerical results because of the scaled numerical setup. The circumferentially and time-averaged profiles are summarized in Fig. 14(*a*) and confirm the positive trend from ME21. All unsteady results show improved results compared to steady RANS. Focusing on MFC, a remarkable agreement of the DDES and experimental data can be seen. The massive separation in the tip region, again, is well resolved by DDES, which explains why this method yields the best agreement. It is worth mentioning, that U-RANS-MFC already shows notable improvements compared to steady RANS, but lacks accuracy in the massively separated tip region and overpredicts this separation size (as illustrated in Fig. 13). This trend is confirmed for the CDN results. While U-RANS still shows an offset to the experiment, DDES get closer to it, but moderately under-predicts the total pressure losses in the tip region, which can be explained with the different mass flow rate for the CDN setups (see Fig. 8). Comparing 2D contours of the stage total pressure ratio in Figs. 14(*b*) to 14(*f*) reveals more details of the flow topology. We identified three essential regions in the experiment, that are captured differently by the simulations. The pressure drop resulting from the stator suction side ①, the pressure peak close to the tip wall influenced by the stator pressure side ② and a region of increased mixing indicated by low and high pressure next to each other in the hub area ③. The DDES-MFC captures all three regions qualitatively. Especially in the tip region, DDES outperforms all other simulations and shows a very good agreement with the contours of the experiment. U-RANS-MFC overpredicts the pressure losses in the tip region. In the hub region, both MFC simulation show comparable results. The CDN simulations, again, follow the respective trend of the method with the mass flow controller, which reflects the results of the circumferentially averaged radial profiles in Fig. 14(*a*). A supplementary illustration, showing the relative deviation of the experiment and DDES-MFC, is provided in Appendix C. Additionally, we show the radial profile of the total temperature at ME30 in Appendix D.

5.4 Comments on computational costs. The increased computational effort of unsteady methods cannot be dismissed, when assessing them comprehensively. A summary of computed non-dimensional time scales and normalized consumed central processing unit hours (CPUh) is given in Tab. 4, which supports future decisions about the appropriate method. This decision is influenced not only by the prediction accuracy, but also by the required computational resources. The stated CPUh values for steady RANS are not related to computed periods and the given range accounts for the various setups and mesh densities considered in this work.

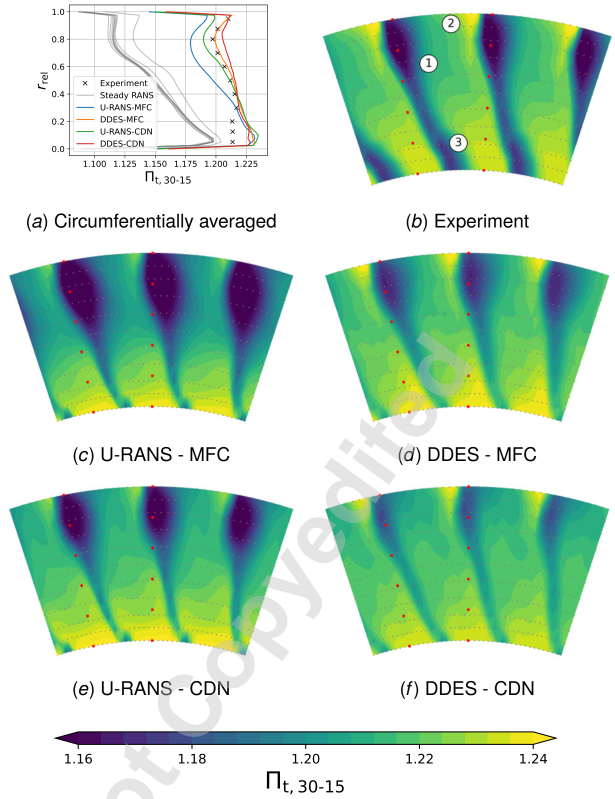

(*a*) Circumferentially averaged (*b*) Experiment

(*c*) U-RANS - MFC (*d*) DDES - MFC

(*e*) U-RANS - CDN (*f*) DDES - CDN

Fig. 14 Time-averaged stage total pressure ratio at ME30 (downstream the stator, see Fig. 2). Simulation data is interpolated on experimental measurement grid, illustrated by grey dot symbols. The red symbols indicate a single passage width, which varies between the experiment and simulations due to different stator vane counts. (a) shows the circumferentially averaged profiles for all methods next to each other.

Especially the largest CPUh value for steady RANS must be considered with caution. It corresponds to the *Ultra-fine* mesh resolution and represents no typical RANS resolution that would be used. The consumed CPUh of the unsteady setups were normalized with the number of computed periods. The notable difference of the CPUh for U-RANS-MFC and -CDN can be explained by a larger time step size (factor 2) that was used for the MFC setup. Otherwise, the CPUh for all other unsteady simulations are in the same range. Even though they are in the same range, it has to be emphasized, that the U-RANS was also applied on a fine setup with respect to the mesh resolution and time step size. Industrial U-RANS setups

Table 4 Summary of computed non-dimensional times scales and computational costs for conducted simulations. The resulting CPUh represent computational costs on a single CPU per period.

Numerical method		t/P	n_{revs}	CPUh / (t/P))
RANS		-	-	37.6 - 2832.0*
U-RANS	MFC	59	3.69	19 736.9
	CDN			37 595.8
DDES	MFC			41 231.1
	CDN			40 585.8

*Note: The CPUh values for steady RANS represents raw CPU hours until the L_1-residual has converged, hence, there is no relation to the number of computed periods. We give a range of CPUh for RANS, which depends on the mesh and operating point control mechanism considered in Sec. 4.

Journal of Turbomachinery. Received May 20, 2026;
Accepted manuscript posted August 10, 2026. doi:10.1115/1.4072497

will likely yield reduced CPUh. Typically, time step sizes of a factor of 8-16 larger are applied and the mesh resolution can also be coarser by at least a factor of 2. This results in an overall reduction in computational cost by a factor of approximately 16-32. A justification for the used U-RANS setups in this study was given in Sec. 5. To determine a ratio of CPUh required by RANS and DDES, the numbers for the DDES have to be multiplied by the computed periods.

It was demonstrated, that the DDES is a very powerful method to compute this off-design operating point, but it also comes with increased computational costs (compared to RANS), which becomes even more significant once a full-annulus (required if the real blade count of 16 rotor blades and 29 stator vanes is considered) or multi-stage applications are computed. Nevertheless, compared to LES (as also shown in [32,45] or can be approximated by the reported numbers in [46] combined with the Reynolds number scaling by Choi and Moin [47]) the DDES is still notably cheaper and poses a powerful compromise between accuracy and costs.

6 Conclusions

The TU Darmstadt axial compressor stage was investigated for an off-design operating point near stall. Therefore, different numerical approaches such as steady and unsteady time-domain RANS methods as well as the hybrid RANS/LES method DDES were used to assess the capabilities and limitations of each approach. Since these operating conditions are characterized by high unsteadiness, different control mechanisms of the mass flow rate are compared and assessed in terms of applicability and reliability. The importance of the combination of capturing unsteady flow phenomena at all and resolving them with a higher-fidelity method, such as DDES, was demonstrated in this work. With regard to the research questions formulated above, the following conclusions can be drawn:

- At near stall conditions, the inherent unsteadiness of the flow field pushes steady RANS to its limits and the deviations to experimental data were large. A fixed static outlet pressure BC to control the operating point cannot be used to approach near stall conditions. The mass flow controller and a converging-diverging nozzle yield comparable results. Additionally, the mesh density variation resulted in increased deviations with refined meshes and a turbulence model extension variation emphasized the sensitivity of these extensions to the capabilities to simulate near stall conditions. These results led to the conclusion that unsteady methods are required to accurately predict this operating point.

- The comparison of U-RANS and DDES highlighted the capabilities of using unsteady methods near stall. Although U-RANS has already shown significant improvements in predicting the integral stage total pressure ratio, discrepancies were identified in radial profiles and 2D contours. The DDES method showed remarkable agreement with the experiment, not only the integral operating point in the performance map, but also 1D and 2D data at the measurement locations. Reasons for this were given by the ability to capture the unsteady processes in the rotor and stator passage, when resolving a large amount of turbulent scales. While U-RANS is capable of capturing the deterministic scales of the unsteady flow field, DDES benefits from resolving also a large amount of stochastic scales. It was demonstrated that this hybrid RANS/LES approach is a very powerful method to simulate off-design conditions with improved accuracy.

- The mass flow controller has emerged as an effective control mechanism yielding the correct mass flow rate oscillating around the target value. Both U-RANS and DDES yield the largest improvements in terms of predicted pressure rise based on this control approach. The converging-diverging nozzle geometry was derived based on ideal gas relations and RANS precursor simulations, which is critical if the steady approach shows large deviations to the experiment. Once the unsteady methods capture more flow characteristics, the nozzle geometry does not fit to the target mass flow rate anymore and a different operating point is approached. Based on these findings, the MFC approach is the most suitable method for such near stall operating point, because it does not require *a priori* knowledge to derive the correct geometry and no iterations to meet the target operating point.

Even though DDES produced very accurate results, it has to be mentioned that this method also comes with increased computational effort. Therefore, the engine designer must decide wisely on whether or not this more expensive method is appropriate to answer a specific aerodynamic question. The results and CPUh presented in this work are intended to inform this decision. As a logical next step, the DDES with an adjusted nozzle geometry could be conducted to realize the targeted near stall mass flow rate. Additionally, the setup could be extended to include multiple rotor passages. This would enable the interaction between adjacent passages, allowing phenomena such as rotating stall at off-design operating conditions to be captured. Further, the DDES setup was generated based on best-practice guideline regarding the spatial and temporal resolution. It would be valuable to analyze how this method performs on even coarser setups.

Acknowledgment

The authors gratefully acknowledge the scientific support and HPC resources provided by the German Aerospace Center (DLR), which enabled us to run the simulations. The HPC system CARA[5] is partially funded by "Saxon State Ministry for Economic Affairs, Labour and Transport" and "Federal Ministry for Economic Affairs and Energy". The HPC system CARO[6] is partially funded by "Ministry of Science and Culture of Lower Saxony" and "Federal Ministry for Economic Affairs and Energy". Other than that, this research did not receive any specific grant from funding agencies in the public, commercial, or non-for-profit sectors.

Nomenclature

Roman letters

A_{crit} = critical cross-section of the outlet nozzle [m^2]
c_{ax} = axial chord length [m]
f_{c} = characteristic frequency [s^{-1}]
k_{res} = resolved turbulent kinetic energy [m^2 s^{-2}]
l_{t} = turbulent length scale [m]
Ma = Mach number [-]
$\dot{m}$ = mass flow [kg m^{-3}]
N = rotational speed [rpm]
n_{cells} = number of cells [-]
n_{rev} = number of computed revolutions [-]
n_{tspp} = number of time steps per period [-]
p_{s} = static pressure [Pa]
p_{t} = total pressure [Pa]
P = duration of a single period [s]
r_{rel} = relative radius [-]
T_{t} = total temperature [K]
t = physical time [s]
u_i = Cartesian velocity vector [m s^{-1}]
u_{mag} = velocity magnitude [m s^{-1}]
x, y, z = Cartesian coordinates [m]

Greek letters

α = circumferential flow angle [deg]
γ = intermittency factor [-]

[5] https://www.top500.org/system/179779 (accessed on 23.06.2026)
[6] https://www.top500.org/system/180038 (accessed on 23.06.2026)

Journal of Turbomachinery. Received May 20, 2026;
Accepted manuscript posted August 10, 2026. doi:10.1115/1.4072497

Δ_{SLS} = sub-grid length scale [m]
$\Delta\xi^+, \eta^+, \Delta\zeta^+$ = non-dimensional cell sizes [-]
δ = radial surface displacement [m]
η_{is} = isentropic efficiency [-]
κ = specific heat capacity ratio [-]
Π_{t} = total pressure ratio [-]
σ_{b} = blending factor [-]
ϕ_{relax} = relaxation factor [-]
ω_{sw} = streamwise vorticity [s^{-1}]

Subscripts

corr = corrected value to ISA conditions
out = value at outlet panel
real = actual value derived from ISA conditions
rel = relative value
ISA = reference value at ISA conditions
15 = value at ME15
21-15 = ratio between ME21 and ME15
30-15 = ratio between ME30 and ME15

Appendix A: Steady RANS convergence

Figure A.1 shows the convergence of steady RANS simulations for all three operating point control mechanisms at the considered near stall operating point. They are exemplarily shown for GF=1.0 (see Tab. 2). It becomes clear that the fixed outlet pressure BC converges towards a lower level of the L_1 and $L_{\max}$ residuals. The mass flow controller and converging-diverging nozzle show more pronounced oscillations and do not converge as low as FOP.

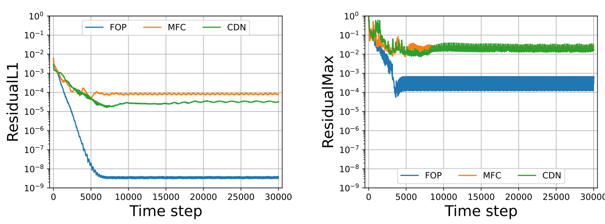

(*a*) Residual L_1 (*b*) Residual $L_{\max}$

Fig. A.1 Different residuals showing the state of convergence for steady RANS simulations for all three control mechanisms at near stall conditions.

Appendix B: Comparison of the resolved turbulent kinetic energy at ME30

The improvements of DDES for predicting the separated tip region can be explained with Fig. B.1, showing the normalized resolved turbulent kinetic energy. It becomes clear that DDES captures a larger amount of resolved turbulent scales, which U-RANS does not. Additionally, the center of maximum turbulent kinetic energy is different, where U-RANS shows a shift to the mid-span region of the passage.

Appendix C: Relative deviation of the total pressure ratio at ME30

The trends for the 1D and 2D distribution at ME30 (shown in Fig. 14) are supplemented by Fig. C.1 showing the relative deviation of $\Pi_{\mathrm{t,30\text{-}15}}$ exemplarily for DDES-MFC. It becomes clear that at most radial positions, the positive and negative deviation is balanced, hence, the circumferentially averaged values collapse with the experimental reference. Only for $r_{\mathrm{rel}} \leq 0.25$, a more pronounced region of positive relative deviation is apparent, which explains the larger differences, also seen in Fig. 14(*a*). The marginal differences in circumferential direction at constant radius can be explained with the fact, that the experiment considers a full annulus, hence, shows variations in each single passage. The numerical approach assumes periodicity in circumferential direction.

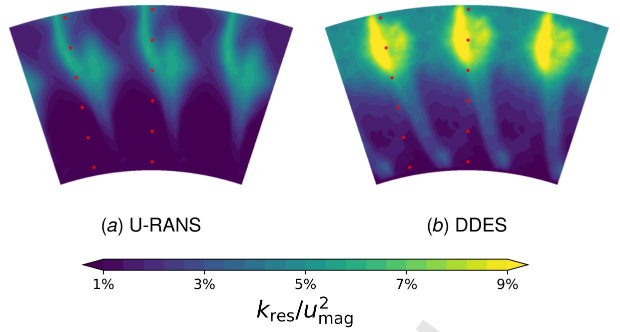
(*a*) U-RANS (*b*) DDES

Fig. B.1 Normalized resolved turbulent kinetic energy at ME30 for U-RANS and DDES both simulated with the mass flow controller. Red symbols indicate the width of a single passage for the numerical domain, whereas the distance between each symbol pair is equivalent to 20% relative radius.

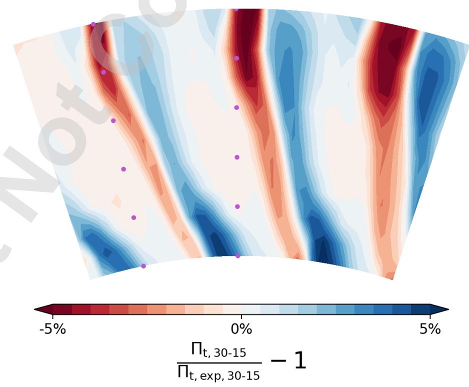

Fig. C.1 Relative deviation of the total pressure ratio at ME30 exemplarily shown for DDES-MFC. Purple symbols indicate the width of a single passage for the numerical domain, whereas the distance between each symbol pair is equivalent to 20% relative radius.

Appendix D: Supplementary radial profiles

Figure D.1 shows the circumferential flow angle α at ME21. Steady RANS is not capable of predicting this value correctly, while showing large underprediction in the hub region until mid-span. This shifts into a notable overprediction in the tip region of the blade. Capturing the accurate flow angle is essential in the turbomachinery design process as this determines the inflow angle for the downstream blade row. Hence, a good row- or stage-matching can only be guaranteed, if the numerical method reliably provides results. Consequently, all unsteady simulations show improvements and get closer to the experimental reference data. Resolving the unsteady flow field with higher accuracy is beneficial to capture the correct flow angle, which is done best by DDES-MFC.

Another important design parameter is the total temperature ratio $T_{\mathrm{t,30\text{-}15}}$, shown in Fig. D.2 for ME30. For this variable, the relative measurement error is derived based on the theory of uncertainty propagation. The test case summary [14] provides absolute errors for the used equipment at the respective measurement location, which allows an approximation of experimental uncertainties. While steady RANS consistently fails, differences between

Journal of Turbomachinery. Received May 20, 2026;
Accepted manuscript posted August 10, 2026. doi:10.1115/1.4072497

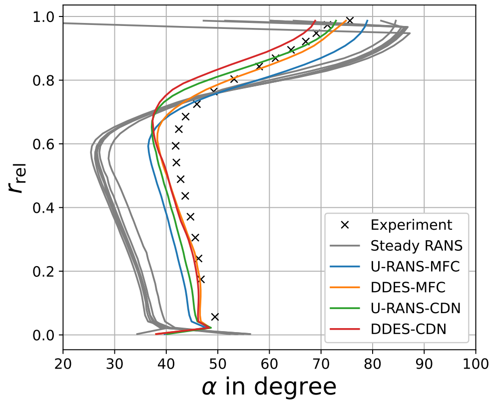

Fig. D.1 Radial profiles of the circumferential flow angle at ME21.

the unsteady simulation occur. Both U-RANS simulations show a change in the profile shape at $x_{\mathrm{rel}} = 0.7$, which is not seen by the DDES. This shape change is even more pronounced in the steady RANS simulations. DDES captures the radial re-distribution of work more accurately and shows better agreement with the experiment. Overall, the DDES-MFC best matches the experiment, qualitatively.

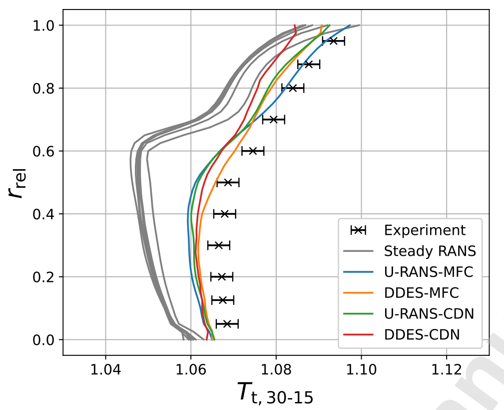

Fig. D.2 Radial profiles of the total temperature ratio at ME30. Experimental data is shown with an approximated relative error based on given accuracies in [14].

References

[1] Denton, J. D., 2010, "Some Limitations of Turbomachinery CFD," *Volume 7: Turbomachinery, Parts A, B, and C*, ASMEDC, Glasgow, UK, pp. 735–745, doi: 10.1115/gt2010-22540.

[2] Montomoli, F., Carnevale, M., D'Ammaro, A., Massini, M., and Salvadori, S., 2015, *Limitations in Turbomachinery CFD*, Springer International Publishing, pp. 21–32.

[3] Tyacke, J., Vadlamani, N., Trojak, W., Watson, R., Ma, Y., and Tucker, P., 2019, "Turbomachinery simulation challenges and the future," Progress in Aerospace Sciences, **110**, p. 100554.

[4] Bergmann, M., Morsbach, C., Klose, B. F., Ashcroft, G., and Kügeler, E., 2023, "A Numerical Test Rig for Turbomachinery Flows Based on Large Eddy Simulations With a High-Order Discontinuous Galerkin Scheme—Part I: Sliding Interfaces and Unsteady Row Interactions," Journal of Turbomachinery, **146**(2), p. 021005.

[5] Klose, B. F., Morsbach, C., Bergmann, M., Hergt, A., Klinner, J., Grund, S., and Kügeler, E., 2023, "A Numerical Test Rig for Turbomachinery Flows Based on Large Eddy Simulations With a High-Order Discontinuous Galerkin Scheme—Part II: Shock Capturing and Transonic Flows," Journal of Turbomachinery, **146**(2), p. 021006.

[6] Morsbach, C., Bergmann, M., Tosun, A., Klose, B. F., Bechlars, P., and Kügeler, E., 2023, "A Numerical Test Rig for Turbomachinery Flows Based on Large Eddy Simulations With a High-Order Discontinuous Galerkin Scheme—Part III: Secondary Flow Effects," Journal of Turbomachinery, **146**(2), p. 021007.

[7] Sandberg, R. D. and Michelassi, V., 2019, "The Current State of High-Fidelity Simulations for Main Gas Path Turbomachinery Components and Their Industrial Impact," Flow, Turbulence and Combustion, **102**(4), pp. 797–848.

[8] Gan, J., Im, H.-S., and Zha, G.-C., 2016, "Delayed Detached Eddy Simulation of Rotating Stall for a Full Annulus Transonic Axial Compressor Stage," *Volume 2A: Turbomachinery*, American Society of Mechanical Engineers, p. 57985, doi: 10.1115/gt2016-57985.

[9] Yamada, K., Furukawa, M., Tamura, Y., Saito, S., Matsuoka, A., and Nakayama, K., 2017, "Large-Scale Detached-Eddy Simulation Analysis of Stall Inception Process in a Multistage Axial Flow Compressor," Journal of Turbomachinery, **139**(7), p. 071002.

[10] Scheibel, J., Stößel, M., and Kožulović, D., 2025, "Pre-stall prediction of a transonic engine compressor based on URANS and hybrid RANS/LES methodology," *Proceedings of THMT-25 Turbulence, Heat and Mass Transfer 11, 21-25 July 2025, Tokyo, Japan*, Begellhouse, p. 8, doi: 10.1615/thmt-25.410.

[11] Scheibel, J. A., Schäfer, Y., Stößel, M., and Kožulović, D., 2025, "Full Annulus Hybrid RANS/LES Prestall Prediction of Transonic Axial Compressor Compared to Real Engine Data," *17th International Symposium on Unsteady Aerodynamics Aeroacoustics and Aeroelasticity of Turbomachines*, pp. 17–053.

[12] Patel, P., Yang, Y., and Zha, G., 2020, "Improved Delayed Detached Eddy Simulation (IDDES) of a 1.5 Stage Axial Compressor Non-Synchronous Vibration," *Volume 10A: Structures and Dynamics*, American Society of Mechanical Engineers, p. 15073, doi: 10.1115/gt2020-15073.

[13] Bakhtiari, F., Wartzek, F., Leichtfuß, S., Schiffer, H.-P., Goinis, G., and Nicke, E., 2015, "Design and Optimization of a New Stator for the Transonic Compressor Rig TU Darmstadt," *Deutscher Luft- und Raumfahrtkongress 2015*, pp. 1–10.

[14] Klausmann, F., Franke, D., Foret, J., and Schiffer, H.-P., 2022, "Transonic compressor Darmstadt - Open test case Introduction of the TUDa open test case," Journal of the Global Power and Propulsion Society, **6**, pp. 318–329.

[15] Klausmann, F. S., Kilian, N., He, X., Spieker, D., Schmidt, B., and Schiffer, H.-P., 2024, "Transonic Compressor Darmstadt Open Test Case: Experimental Investigation of Stator Secondary Flows and Hub Leakage," Journal of Turbomachinery, **146**(10), p. 101007.

[16] Giles, M., 1991, "UNSFLO: A Numerical Method For The Calculation Of Unsteady Flow In Turbomachinery," *Technical Report, Gas Turbine Laboratory*, pp. 1–91.

[17] Schlüß, D., Frey, C., and Ashcroft, G., 2016, "Consistent Non-Reflecting Boundary Conditions For Both Steady And Unsteady Flow Simulations In Turbomachinery Applications," *7th European Congress on Computational Methods in Applied Sciences And Engineering*, pp. 1–20, https://eccomas2016.org/proceedings/pdf/5411.pdf

[18] Yang, H., Nürnberger, D., and Weber, A., 2002, "A Conservative Zonal Approach with Application to Unsteady Turbomachinery Flows," *DGLR Jahrestagung*, pp. 1–10.

[19] Bode, C., Przytarski, P. J., Leggett, J., and Sandberg, R. D., 2022, "Highly Resolved Large-Eddy Simulations of a Transonic Compressor Stage Midspan Section Part I: Effect of Inflow Disturbances," *Volume 10D: Turbomachinery — Multidisciplinary Design Approaches, Optimization, and Uncertainty Quantification; Turbomachinery General Interest; Unsteady Flows in Turbomachinery*, American Society of Mechanical Engineers, p. 81673, doi: 10.1115/gt2022-81673.

[20] He, X., Zhu, M., Xia, K., Fabian, K., Teng, J., and Vahdati, M., 2023, "Validation and verification of RANS solvers for TUDa-GLR-OpenStage transonic axial compressor," Journal of the Global Power and Propulsion Society, **7**, pp. 13–29.

[21] Department of Numerical Methods, 2016, *PyMesh - Meshing Package for Turbomachinery CFD - Template Documentation*, DLR-Institute of Propulsion Technology.

[22] He, X. and Klausmann, F., 2024, "RANS Capabilities for Transonic Axial Compressor: A Perspective from GPPS CFD Workshop," Journal of Turbomachinery, pp. 1–32.

[23] Matha, M., Möller, F. M., Bode, C., Morsbach, C., and Kügeler, E., 2025, "Advanced Methods for Assessing Flow Physics of the TU Darmstadt Compressor Stage: Uncertainty Quantification of RANS Turbulence Modeling," Journal of Turbomachinery, **147**(8), p. 081004.

[24] Department of Numerical Methods, 2017, "TRACE Suite," DLR-Institute of Propulsion Technology, doi: 10.5281/zenodo.17749324.

[25] Geiser, G., Wellner, J., Kügeler, E., Weber, A., and Moors, A., 2019, "On the Simulation and Spectral Analysis of Unsteady Turbulence and Transition Effects in a Multistage Low Pressure Turbine," Journal of Turbomachinery, **141**(5), p. 051012.

[26] Ashcroft, G., Frey, C., Heitkamp, K., and Weckmüller, C., 2013, "Advanced Numerical Methods for the Prediction of Tonal Noise in Turbomachinery—Part I: Implicit Runge–Kutta Schemes," Journal of Turbomachinery, **136**(2), p. 021002.

[27] Möller, F. M., Tucker, P. G., Wang, Z.-N., Bode, C., Morsbach, C., Matha, M., and Sivel, P., 2024, "Advanced Methods for Assessing Flow Physics of the TU Darmstadt Compressor Stage: Part 1 – Transitional Delayed Detached-Eddy Simulation," *Volume 12C: Turbomachinery — Design Methods and CFD Modeling for Turbomachinery; Ducts, Noise, and Component Interactions*, American Society of Mechanical Engineers, p. 127679, doi: 10.1115/gt2024-127679.

[28] Menter, F., Kuntz, M., and Langtry, R., 2003, "Ten Years of Industrial Experience with the SST Turbulence Model," Turbulence, Heat and Mass Transfer, **4**, pp. 625–632.

Journal of Turbomachinery. Received May 20, 2026;
Accepted manuscript posted August 10, 2026. doi:10.1115/1.4072497

[29] Menter, F. R., Smirnov, P. E., Liu, T., and Avancha, R., 2015, "A One-Equation Local Correlation-Based Transition Model," Flow, Turbulence and Combustion, **95**(4), pp. 583–619.

[30] Möller, F. M., Tucker, P. G., Wang, Z.-N., Morsbach, C., and Bergmann, M., 2023, "On the Prediction of Separation-Induced Transition by Coupling Delayed Detached-Eddy Simulation with γ-Transition Model," *15th European Conference on Turbomachinery Fluid Dynamics and Thermodynamics*, European Turbomachinery Society, p. 375, doi: 10.29008/etc2023-375.

[31] Möller, F. M., Tucker, P. G., Wang, Z.-N., and Morsbach, C., 2024, "Transitional Delayed Detached-Eddy Simulation for a Compressor Cascade: A Critical Assessment," Journal of Propulsion and Power, **40**(4), pp. 533–546.

[32] Möller, F. M., Bergmann, M., Morsbach, C., Tucker, P. G., Wang, Z.-N., Hergt, A., and Herbst, F., 2025, "Reynolds Number Effect on Transitional Delayed Detached-Eddy Simulation," Journal of Turbomachinery, **148**(2), p. 021005.

[33] Spalart, P. R., Deck, S., Shur, M. L., Squires, K. D., Strelets, M. K., and Travin, A., 2006, "A New Version of Detached-eddy Simulation, Resistant to Ambiguous Grid Densities," Theoretical and Computational Fluid Dynamics, **20**(3), pp. 181–195.

[34] Shur, M. L., Spalart, P. R., Strelets, M. K., and Travin, A. K., 2015, "An Enhanced Version of DES with Rapid Transition from RANS to LES in Separated Flows," Flow, Turbulence and Combustion, **95**(4), pp. 709–737.

[35] Travin, A., Shur, M., Strelets, M., and Spalart, P. R., 2002, "Physical and Numerical Upgrades in the Detached-Eddy Simulation of Complex Turbulent Flows," *Fluid Mechanics and Its Applications: Advances in LES of Complex Flows*, Springer Netherlands, pp. 239–254.

[36] Roe, P., 1981, "Approximate Riemann solvers, parameter vectors, and difference schemes," Journal of Computational Physics, **43**(2), pp. 357–372.

[37] Saravanamuttoo, H. I. H., Rogers, G. F. C., and Cohen, H., 2001, *Gas turbine theory*, 5th ed., Prentice Hall.

[38] Becker, K., Geihe, B., Ashcroft, G., and Schoenenborn, H., 2018, "On the numerical simulation of a surge cycle using a quasi-unsteady mixing plane," *Proceedings of the Global Power and Propulsion Forum*, GPPS, pp. 2018–0105.

[39] Möller, D. and Schiffer, H.-P., 2021, "On the Mechanism of Spike Stall Inception and Near Stall Nonsynchronous Vibration in an Axial Compressor," Journal of Engineering for Gas Turbines and Power, **143**(2), p. 021007.

[40] Kato, M. and Launder, B., 1993, "The modeling of turbulent flow around stationary and vibrating square cylinders," *9th Symposium on Turbulent Shear Flows*, Kyoto, Japan, pp. 10.4.1–10.4.6.

[41] Bardina, J., Ferziger, J. H., and Rogallo, R. S., 1985, "Effect of rotation on isotropic turbulence: computation and modelling," Journal of Fluid Mechanics, **154**, pp. 321–336.

[42] Tucker, P., 2014, *Unsteady Computational Fluid Dynamics in Aeronautics*, Springer Netherlands.

[43] Bergmann, M., Morsbach, C., Ashcroft, G., and Kügeler, E., 2021, "Statistical Error Estimation Methods for Engineering-Relevant Quantities From Scale-Resolving Simulations," Journal of Turbomachinery, **144**(3), p. 031005.

[44] Hunt, J., Wray, A., and Moin, P., 1988, "Eddies, Streams, and Convergence Zones in Turbulent Flows," *Studying Turbulence Using Numerical Simulation Databases, 2nd Proceedings of the 1988 Summer Programm*, pp. 193–208, https://ntrs.nasa.gov/citations/19890015184

[45] Wang, Z.-N. and Tucker, P. G., 2023, "Hierarchical Turbulence and Geometry Modeling: Case Study for Fan Stage Flows," AIAA Journal, **61**(7), pp. 2824–2839.

[46] Morsbach, C., Klose, B. F., Bergmann, M., and Möller, F. M., 2024, *Modal Analysis of High-Fidelity Simulations in Turbomachinery*, Springer Nature Switzerland, pp. 103–119.

[47] Choi, H. and Moin, P., 2012, "Grid-point requirements for large eddy simulation: Chapman's estimates revisited," Physics of Fluids, **24**(1), p. 011702.

Journal of Turbomachinery. Received May 20, 2026;
Accepted manuscript posted August 10, 2026. doi:10.1115/1.4072497

List of Figures

List of Tables